Optical pumping and spectroscopy of Cs vapor at high magnetic field

B. A. Olsen,[*] B. Patton,[†] Y.-Y. Jau,[‡] and W. Happer
Joseph Henry Laboratory, Department of Physics, Princeton University, Princeton, New Jersey 08544, USA
(Received 4 October 2011; published 7 December 2011)

We have measured changes in the ground-state populations of Cs vapor induced by optical pumping at high magnetic field. The 2.7-T field of our experiments is strong enough to decouple the nuclear and electronic spins, allowing us to independently measure each population. The spatial dependence of the Cs populations in small amounts of buffer gas obeys a simple coupled diffusion model and the relative populations reveal the details of relaxation within the vapor cell. Optical pumping can produce high nuclear polarization in the Cs vapor due to perturbations of the hyperfine interaction during collisions with buffer-gas particles and depending on the pumping transition, radiation trapping can strongly influence the electronic and nuclear polarizations in the vapor.

DOI: 10.1103/PhysRevA.84.063410 PACS number(s): 32.80.Xx, 32.60.+i, 32.50.+d, 32.10.Fn

I. INTRODUCTION

Alkali-metal vapor cells are widely used in both basic and applied research. In vapor-cell experiments and technologies, a warm alkali-metal vapor is contained in a glass cell and subsequently manipulated with light to induce spin polarization. Interactions at the cell walls quickly relax both the nuclear and electronic spins in the alkali-metal vapor, reducing the maximum polarization [1–3]. Vapor cells are commonly filled with buffer gases to decrease the rate at which polarized alkali-metal atoms collide with the cell walls. Considerable effort has been devoted to miniature vapor cells, where depolarization at the walls plays an especially important role [4–8].

Although optical pumping is typically performed at low (<100 G) magnetic fields, high-field optical pumping has played a long-standing role in the investigation of buffer-gas-induced electron-spin relaxation in alkali-metal atoms. In early experiments, researchers measured the magnetic field decoupling of these relaxation rates for Cs-Ne and Cs-He; such investigations revealed the correlation times of the binary alkali-metal–noble-gas interactions [9–11]. More recently, high-field optical pumping allowed spin-exchange interactions between an alkali-metal vapor and noble-gas nuclei to be studied in a similar fashion [12,13].

In early experiments at high magnetic field, researchers optically pumped the alkali-metal vapor with white light and measured electronic-spin-relaxation times [9,10]. Other researchers measured the magnetic-field dependence of relaxation in optically pumped alkali-metal vapors with noble buffer gases [11]. More recently, researchers characterized the transfer of polarization from an optically pumped alkali-metal vapor to noble-gas nuclei in magnetic fields with high enough strength to decouple the electronic and nuclear spins in the alkali-metal vapor [12,13].

In recent experiments, Ishikawa *et al.* transferred polarization from an optically pumped Cs vapor to the nuclear spins of Cs salts on the walls of vapor cells at high magnetic field [14]. Further work by Ishikawa *et al.* showed that the enhancement of the polarization in the salt was dominated by nuclear-spin polarization in the vapor [15]. Polarization enhancement in the salt depends on the alkali-metal vapor, on surface interactions, and on spin dynamics in the salt. Our goal in this work is to quantify the nuclear and electronic polarizations produced in the optically pumped vapor.

Polarization transfer from an optically pumped vapor to nuclei on the cell wall can dramatically increase the signal-to-noise ratio of a nuclear magnetic resonance (NMR) experiment since it allows the nuclei to be polarized to a much higher degree than the Boltzmann equilibrium. However, high-field optical pumping of free alkali-metal atoms on allowed optical transitions produces much more electronic- than nuclear-spin polarization [16]. Since nuclear-spin-polarized atoms are much more efficient at transferring spin polarization to nuclei in the wall [17], ways are needed to enhance the nuclear-spin polarization in the optically pumped vapor. In this paper we discuss two enhancement methods.

(i) Optical pumping on forbidden transitions can polarize the nuclear spins directly, with results similar to the Overhauser effect [18].

(ii) Collisions with buffer gases, which cause large modifications of the hyperfine coupling coefficients of the gas-phase atoms, can greatly increase the nuclear-spin polarization.

The field strength required for decoupling of the nuclear and electronic spins is given by $B \gg A/\mu_B \approx 0.2$ T for Cs, where A is the ground-state hyperfine coupling coefficient and μ_B is the Bohr magneton. At such high magnetic fields, the electron Zeeman interaction dominates and splits the ground-state energy levels of the alkali-metal atom (with electronic- and nuclear-spin quantum numbers S and I, respectively) into two manifolds with electron-spin projections $m_S = \pm\frac{1}{2}$. Both manifolds consist of $2I + 1$ sublevels separated by the ground-state hyperfine splitting $A_{S_{1/2}}/2$. In Cs, the two m_S manifolds are separated by 75.7 GHz at 2.7 T and the eight sublevels in each manifold are spread over roughly 10 GHz (see Fig. 1). Similar high-field conditions prevail in the $P_{1/2}$ and $P_{3/2}$ excited states.

[*]bolsen@alumni.princeton.edu
[†]Present address: Department of Physics, University of California, Berkeley, CA 94720, USA.
[‡]Present address: Sandia National Laboratories, Albuquerque, NM 87185-1082, USA.

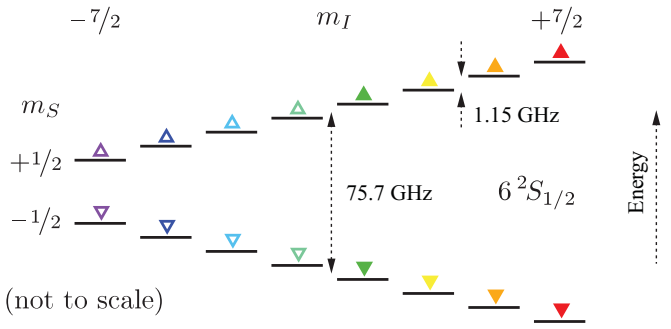

FIG. 1. (Color online) Ground-state energy levels of Cs vapor at a magnetic field of 2.7 T, as used in our experiments. The two manifolds with $m_S = \pm\frac{1}{2}$ are separated by a Zeeman energy of 75.7 GHz. Each manifold consists of eight sublevels, each separated by a hyperfine energy of 1.149 GHz. The sublevels are labeled with colored triangles; the direction of the triangle indicates the electronic spin projection m_S and the color indicates the nuclear spin projection m_I.

In Sec. II we describe experimental measurements of optically pumped Cs vapor in cylindrical glass vapor cells with small amounts of buffer gas at a magnetic field of 2.7 T. We report measurements of the ground-state sublevel populations in the vapor and the nuclear- and electronic-spin projections as functions of position in the cell, pump-laser power, and pump-laser frequency. This technique is similar to recent experiments by Luo *et al.* on optically pumped vapors at high magnetic field [19].

In Sec. III we describe numerical simulations of this optical pumping system. By comparing simulated populations and spin projections to those observed in our experiments, we find that radiation trapping can strongly influence the populations in the vapor and that nuclear-spin polarization in the Cs vapor is mainly determined by the rate of hyperfine-shift collisions with buffer-gas particles.

II. EXPERIMENT

A. Experimental apparatus

To investigate the ground-state populations in an alkali-metal vapor, we designed and built an experimental apparatus to measure absorption spectra of a resonant D_1 ($6\,^2S_{1/2} \rightarrow 6\,^2P_{1/2}$, 894-nm) probe beam passing through a vapor cell. A schematic of this apparatus is shown in Fig. 2. We mounted each vapor cell in a custom nylon holder within a resistively heated cylindrical oven with optical windows. This oven was part of a probe designed for insertion into the room-temperature bore of a superconducting magnet (Oxford Instruments NMR 400). We monitored the temperature of the cell with a pair of resistive temperature sensors placed in loose contact with the walls of the oven and cell.

To polarize the alkali-metal vapor spins, we used a Ti:sapphire ring laser (Coherent 899-21) pumped by a 10-W 532-nm diode-pumped solid-state laser (Coherent Verdi V-10) to produce D_2 ($6\,^2S_{1/2} \rightarrow 6\,^2P_{3/2}$, 852-nm) optical pumping light. We monitored the pump laser frequency with a wavemeter (Exfo WA-1150) and tuned over the various D_2 resonances by adjusting an étalon within the ring laser, which has a spectral

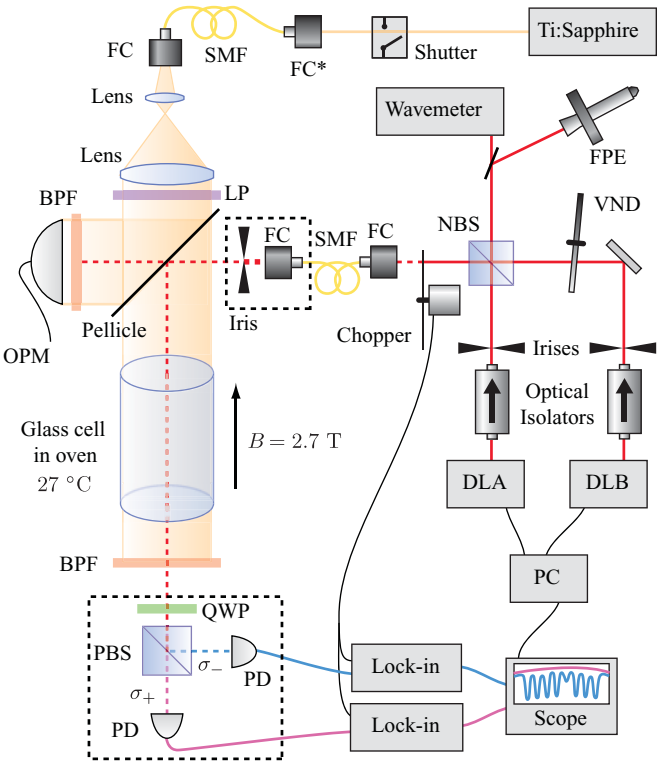

FIG. 2. (Color online) Schematic of our experimental apparatus. Pumping light from a Ti:sapphire laser passed through a single-mode optical fiber (SMF) and was expanded to illuminate the entire vapor cell located in an oven in the bore of a superconducting magnet (not shown). A pellicle reflected part of this beam into an optical power meter (OPM) shielded by a bandpass filter (BPF). The pump beam was linearly polarized using a polaroid sheet (LP). Two diode lasers (DLA, DLB) produced the probe light; we blocked one beam while performing measurements with the other. We controlled the relative intensities using a variable neutral-density filter (VND) and overlapped the two beam paths with a nonpolarizing beam-splitter cube (NBS). We measured the optical frequencies with a wavemeter and scanning Fabry-Pérot étalon (FPE) and modulated the probe intensity with a mechanical chopper. Both pump and probe beams were coupled into single-mode optical fibers (SMF) using fiber couplers (FC). The regions outlined in dashed boxes translated into and out of the page to perform spectroscopic measurements at several positions along a diameter of the cylindrical cell. The probe beam was linearly polarized before passing through the cell; we measured the transmitted intensities of σ_+ and σ_- light with a $\lambda/4$-plate (QWP) and polarizing beam splitter (PBS) with outputs monitored by two photodetectors (PD) read with lock-in amplifiers and transmitted to a desktop computer (PC).

width less than 1 MHz. The laser light passed through a computer-controlled optical shutter and was routed through a single-mode optical fiber to the top of the probe. The beam was expanded to illuminate the entire vapor cell and this light was linearly polarized with a polaroid sheet below the second lens. Part of this beam was reflected off a tilted pellicle into an optical power meter with an area of 1 cm^2 (Newport 818-SL) with a bandpass filter to measure the intensity of pumping light.

We adjusted the pump beam power by decreasing the input coupling efficiency for the single-mode optical fiber connecting to the top of the probe, typically until the power meter

on the probe read 0.20 ± 0.01 mW. This power was smaller than the maximum we could achieve with the laser; since changing the laser's frequency also changed its maximum output power, we wanted to ensure that we could maintain the same power at all pump frequencies.

We performed absorption spectroscopy of the alkali-metal vapor using a weak D_1 laser beam. Two tunable external-cavity diode lasers in Littrow configuration (Toptica DL100) produced the probe light. We swept the frequencies of the two probe lasers over about 10 GHz across the transitions D_1(a) and D_1(d) (see Fig. 5). One laser swept over the D_1(a) resonances and the other over the D_1(d) resonances to improve the speed and reliability of the measurements. During each measurement, we blocked one beam and used the other to probe the vapor.

We combined the two probe beam paths with a non-polarizing beam splitter. We sent one output of the beam splitter to a Fabry-Pérot étalon and wavemeter to monitor the probe frequency. Using a chopper, we modulated the intensity of the other output at a frequency of 310 Hz and routed this modulated beam to the probe assembly with a single-mode optical fiber with a core diameter of 4 μm (Oz Optics SMJ-3AF3S-633-4/125-3-5). The resulting beam reflected off of the pellicle near the top of the probe and passed through the atomic vapor. The resulting probe beam was weak enough ($\approx$50 nW/cm^2) not to perturb the atomic vapor.

Since both the pump and probe beams propagated along the magnetic field, no π-polarized light could be sent to the cell and the linearly polarized pump and probe beams could be resolved into their σ_+ and σ_- components. Below the cell we attenuated the D_2 beam by a factor of 10^5 with an interference bandpass filter (Asahi Spectra Co. ZBPA900), which transmitted about half of the D_1 probe beam. We detected the intensities I_{+1}, I_{-1} of σ_+,σ_- light in the probe beam, respectively, using two amplified photodiodes and lock-in amplifiers (Stanford Research Systems SR830 and SR850). We recorded the output of those amplifiers on an oscilloscope (Tektronix TDS3034). This modulated detection scheme reduced noise due to residual pump beam intensity transmitted through the bandpass filter.

B. Vapor cells

We constructed cylindrical vapor cells from Pyrex glass with radius $R \approx 11$ mm, length $\ell \approx 50$ mm, and optical-quality windows at both ends. Early experiments revealed that these cells significantly distorted the path of an optical probe beam; the cell fabrication process of melting the window and cylinder together produced curvature in the surface of the glass, leading to a lensing effect, as demonstrated in Fig. 3(c). To eliminate lensing near the cylindrical sidewall, we created cells with a dumbbell geometry: windows with $R \approx 15$ mm joined to the cylindrical body of the cell via a curved Pyrex joint, demonstrated in Fig. 3(b). The cylindrical inner wall extends to within 2 mm of the window, so the cell remains nearly cylindrical and eliminates lensing, as demonstrated in Fig. 3(d). We added Cs metal to the cells, filled them with buffer gas, and then sealed them with a procedure similar to that described in Ref. [14].

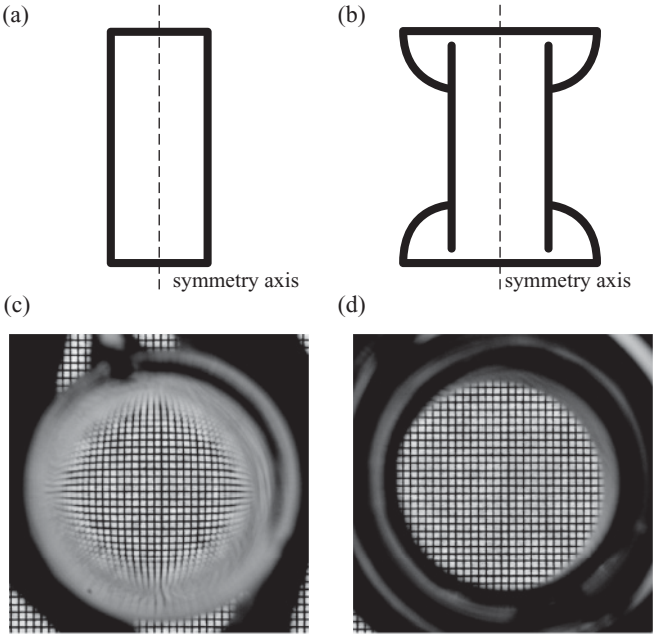

FIG. 3. Cell geometries used in this work: (a) a cross section of a standard cylindrical cell and (b) a cross section of a dumbbell cell created to minimize refraction in the optical windows. The inner cylinder of the dumbbell cell extends to within 2 mm of the optical window at each end. Photographs of a millimeter-scale grid as seen through (c) the conventional cell and (d) the dumbbell cell demonstrate the difference in distortion near the cell walls.

C. Laser spectroscopy

To measure the populations of the sublevels with $m_S = -\frac{1}{2}$, we swept the probe-laser frequency across each of the D_1 transitions with $\Delta m_J = +1$ as shown in Fig. 4, where J is the total electronic angular momentum. Similarly, we measured the sublevel populations with $m_S = +\frac{1}{2}$ by sweeping the frequency of the probe laser across the transitions with $\Delta m_J = -1$.

For an alkali-metal vapor with vanishing coherence, $\rho_{\mu\nu} = 0$ for $\mu \neq \nu$, we can write the average absorption cross section for light with polarization index λ as a sum over ground-state sublevel populations:

$$\langle \sigma_\lambda \rangle = \sum_\mu \sigma_{\mu,\lambda} \langle \rho_{\mu\mu} \rangle, \tag{1}$$

where the absorption cross section $\sigma_{\mu,\lambda}$ for atoms in the ground-state sublevel $|\mu\rangle$ is independent of position. The probability $\rho_{\mu\mu}$ of finding the atom in the sublevel $|\mu\rangle$ will depend strongly on position because of optical pumping and spin relaxation. The mean population $\langle \rho_{\mu\mu} \rangle$ along a beam path of length ℓ is given by

$$\langle \rho_{\mu\mu} \rangle = \frac{1}{\ell} \int_0^\ell \rho_{\mu\mu}(z) dz, \tag{2}$$

where we use a Cartesian coordinate system for which the z axis is along the magnetic field. The cross section $\sigma_{\mu,\lambda}$ for absorption of light with polarization $\mathbf{e}_\lambda$ [$\mathbf{e}_{+1} = -(\hat{\mathbf{x}} + i\hat{\mathbf{y}})/\sqrt{2}$ for σ_+-polarized light, $\mathbf{e}_{-1} = (\hat{\mathbf{x}} - i\hat{\mathbf{y}})/\sqrt{2}$ for σ_--polarized light, and $\mathbf{e}_0 = \hat{\mathbf{z}}$ for π-polarized light; see Eq. (16)] and

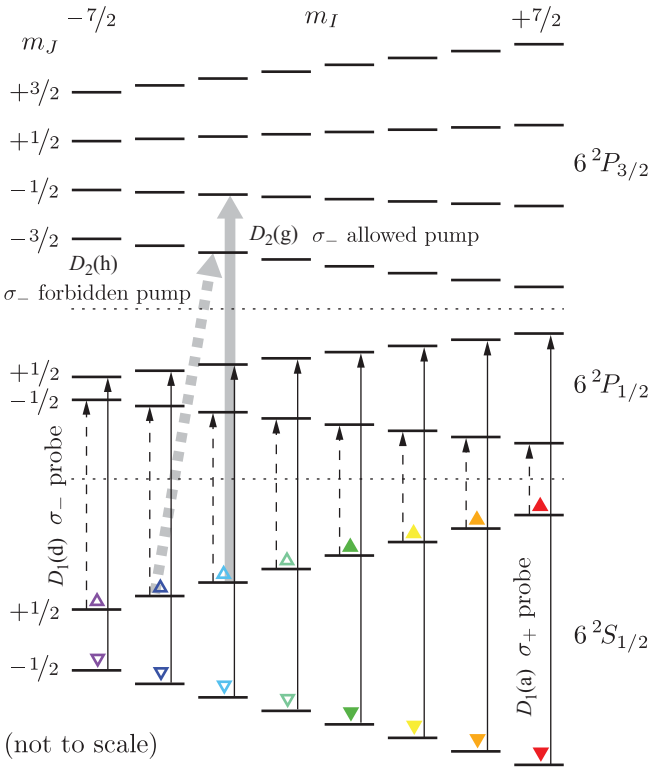

FIG. 4. (Color online) Energy levels of Cs vapor at high magnetic field. Two probe lasers (D_1, $6\,^2S_{1/2} \rightarrow 6\,^2P_{1/2}$, 894 nm) measure the populations of all 16 ground-state sublevels—the manifold $|-\frac{1}{2},m_I\rangle$ with σ_+ light (thin solid arrows) and $|+\frac{1}{2},m_I\rangle$ with σ_- light (thin dashed arrows). The sublevels are denoted by triangles, with upward (downward) triangles indicating $m_S = +\frac{1}{2}$ $(-\frac{1}{2})$ and the color indicating m_I from violet ($m_I = -\frac{7}{2}$) to red ($m_I = +\frac{7}{2}$). A pump beam (D_2, $6\,^2S_{1/2} \rightarrow 6\,^2P_{3/2}$, 852 nm) can be tuned to depopulate any of the ground-state sublevels via allowed and forbidden transitions. Representative allowed and forbidden transitions are depicted with thick solid and dashed arrows, respectively. At high magnetic fields and low buffer-gas pressures, all transitions can be optically resolved.

angular frequency ω by atoms in the ground-state sublevel $|\mu\rangle$ is a sum of contributions from transitions to all excited-state sublevels $|\bar{\mu}\rangle$:

$$\sigma_{\mu,\lambda} = \sum_{\bar{\mu}} \sqrt{\frac{M}{2\pi k_B T}} \frac{4\pi\omega_0\gamma}{\hbar c} \times \int_{-\infty}^{\infty} \frac{|\mathbf{D}_{\bar{\mu}\mu}\cdot\mathbf{e}_\lambda|^2 e^{-Mv^2/2k_BT}}{[\omega-\omega_{\bar{\mu}\mu}(1+v/c)]^2+\gamma^2} dv. \quad (3)$$

Here v, the atomic velocity along the direction of the laser beam, is assumed to have a Maxwellian probability distribution at temperature T, M is the mass of an alkali-metal atom, k_B is Boltzmann's constant, $\hbar$ is the reduced Planck constant, and c is the speed of light. The resonant optical frequencies are $\omega_{\mu\bar{\mu}}$ and their mean value is ω_0. The homogeneous linewidth γ has contributions from the natural lifetime τ and the collisional broadening rate γ_c and is given by $\gamma = 1/2\tau + \gamma_c$. $\mathbf{D}$ is the electric dipole moment operator, and the optical transition frequencies $\omega_{\bar{\mu}\mu} = (E_{\bar{\mu}} - E_\mu)/\hbar + \delta\omega_c$ have small shifts $\delta\omega_c$ due to collisions [see Eq. (8.19) of Ref. [20]]. The convolutions of Lorentzian and Gaussian profiles in Eq. (3) are called Voigt profiles and they can be conveniently evaluated using Faddeeva functions (see Ref. [20], Sec. 6.9).

At finite magnetic fields, the hyperfine interaction mixes the wave functions of sublevels with the same total angular momentum projection $m_I + m_J$. In our numerical simulations, we calculate this mixing exactly, but here we give a perturbation-theory treatment for insight into pumping behavior. At $B = 2.7$ T, the field of our experiments, the energy eigenstates are nearly

$$|\mu\rangle = |m_J,m_I\rangle \pm \epsilon\sqrt{(I\mp m_I)(I\pm m_I+1)} \times |m_J\pm 1, m_I\mp 1\rangle, \quad (4)$$

where $\epsilon = A_g/g_g\mu_B B = 0.030$ in the ground state. Mixing in the excited states is similar, but with smaller ϵ because $A_e \ll A_g$. This small mixing permits the pump light to excite transitions with $\Delta m_I \neq 0$. These singly forbidden transitions obey the relations $\Delta m_I + \Delta m_J = +1$, 0, and -1 for σ_+-, π-, and σ_--polarized light, respectively. According to Eq. (3), $\sigma_{\mu,\lambda} \propto |\mathbf{D}_{\bar{\mu}\mu}\cdot\mathbf{e}_\lambda|^2$. Noting that $\mathbf{D}$ affects only the electronic part of the basis state in Eq. (4), we see that $\sigma_{\mu,\lambda}$ for a singly forbidden transition with excited-state nuclear-spin projection $\bar{m}_I = m_I \pm 1$ will be smaller than $\sigma_{\mu,\lambda}$ for an allowed transition with $\bar{m}_I = m_I$ by a factor of order ϵ^2. A simulation of σ_λ utilizing the fully diagonalized Hamiltonian for Cs in 10 Torr N_2 buffer gas is shown in Fig. 5.

For light with polarization index λ, the intensity $I_\lambda(\ell)$ of probe light after passing through an absorbing vapor of length

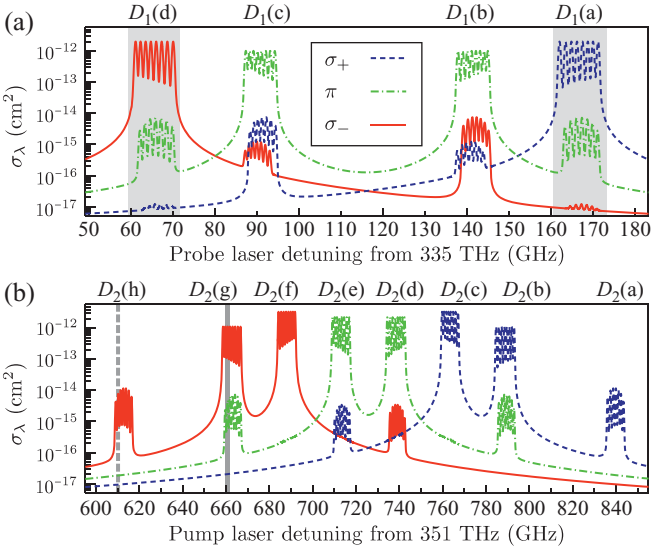

FIG. 5. (Color online) Simulated absorption cross section for unpolarized Cs vapor with Maxwellian velocity distribution at 27 °C and 2.7-T magnetic field in 10 Torr N_2 buffer gas for σ_- [solid (red)], π [dot-dashed (green)], and σ_+ [dashed (blue)] polarizations—note the logarithmic scale on the vertical axis. In (a), the probe beam frequency sweep ranges are indicated by the gray regions. The representative allowed and forbidden pumping transitions of Fig. 4 are indicated by the thick gray solid and dashed lines in (b), respectively. We label multiplets of transitions with letters according to the convention of Ref. [15].

ℓ is related to the average absorption cross section $\langle\sigma_\lambda\rangle$ of the vapor by

$$I_\lambda(\ell) = \Theta I_{\lambda,0}\, e^{-n\ell\langle\sigma_\lambda\rangle}, \tag{5}$$

where Θ is a transmission coefficient due to imperfect optics and $I_{\lambda,0}$ is the intensity the detected beam would have if the number density n of alkali-metal atoms in the vapor vanished and if $\Theta = 1$. To account for variations in the probe-laser intensity, we measured the transmitted intensities $I_{+1}(\ell)$ and $I_{-1}(\ell)$ of σ_+- and σ_--polarized light, respectively, for linearly polarized incident light with initial intensities $I_{+1,0} = I_{-1,0}$. Near the allowed transitions for $\sigma_\pm$ light, the vapor is essentially transparent to light with $\sigma_\mp$ polarization, which has an absorption cross section five orders of magnitude smaller. Near these resonances, we can make the approximation $\langle\sigma_\lambda\rangle - \langle\sigma_{-\lambda}\rangle \approx \langle\sigma_\lambda\rangle$ and we have

$$I_\lambda(\ell)/I_{-\lambda}(\ell) = \Theta' \exp\left(-n\ell \sum_\mu \sigma_{\mu,\lambda}\langle\rho_{\mu\mu}\rangle\right), \tag{6}$$

where Θ' accounts for all experimental imperfections including different gain for the two polarization detector channels. Taking the natural logarithm and inverting the sign, we find the spectrum

$$S_\lambda = -\ln[I_\lambda(\ell)/I_{-\lambda}(\ell)] = n\ell \sum_\mu \sigma_{\mu,\lambda}\langle\rho_{\mu\mu}\rangle + \ln\Theta', \tag{7}$$

which is the sum of eight Voigt profiles and a spurious baseline. The amplitudes of the eight peaks in S_{+1} are proportional to the populations of the sublevels $|-\frac{1}{2},m_I\rangle$; S_{-1} has peak amplitudes proportional to the populations of the sublevels $|+\frac{1}{2},m_I\rangle$. Examples of such spectra are shown in Fig. 6. Since coherences are negligible in our experimental conditions, we can use these two spectra to reconstruct the entire ground-state density matrix of the vapor.

D. Spatial dependence

To measure absorption spectra at different positions within the vapor cell, we moved the probe beam stage above the magnet and the detection optics below the magnet with two mechanical translation stages, acquiring pumped and unpumped spectra with the probe beam at several positions along the diameter of the cylindrical cell. The normalized populations $g_0\langle\rho_{\mu\mu}\rangle = (2I+1)(2S+1)\langle\rho_{\mu\mu}\rangle$ extracted from fits to these spectra are shown in Fig. 7.

In Sec. III we will describe a detailed model for the density-matrix populations that are produced by optical pumping, relaxation, and spatial diffusion. A simplified version of Eq. (12) governs the steady-state deviation $\Delta\rho$ of a single population from its equilibrium value:

$$(D\nabla^2 - \Gamma)\Delta\rho = -P, \tag{8}$$

where the diffusion coefficient D, the total damping rate Γ due to optical pumping and collisions, and the source term P are independent of position. The solutions to this simple diffusion equation in an infinitely long cylinder are given by

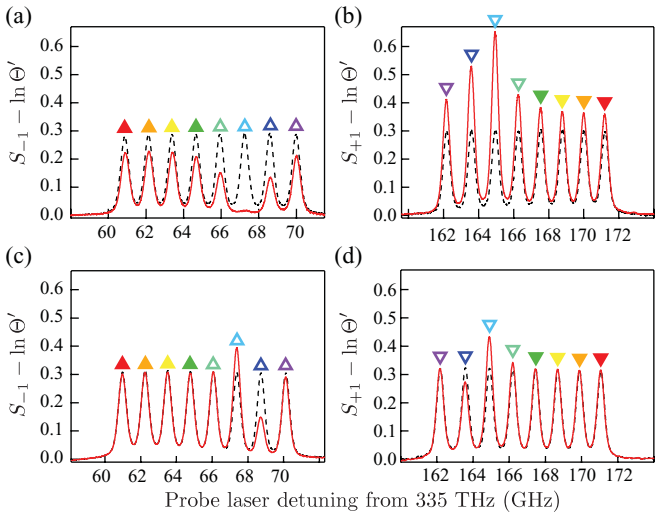

FIG. 6. (Color online) Absorption spectra of Cs vapor in 10 Torr N_2 buffer gas at 27 °C. The probe beam passed through the center of a cylindrical Pyrex cell with $R = 1.1$ cm and $\ell = 5.7$ cm. (a) and (b) show absorption of σ_- and σ_+ probe light, respectively, for pumping on the allowed transition D_2(g) depicted in Fig. 4; (c) and (d) show absorption of σ_- and σ_+ probe light, respectively, for pumping on the forbidden transition D_2(h). The dashed (black) traces show absorption with the pump light off and the solid (red) traces with the pump light on. The triangles identify the ground-state sublevels (see Fig. 4).

the modified Bessel function $I_0(z) = J_0(iz)$ (see Sec. 11.5 of Ref. [21]):

$$\Delta\rho = C I_0(r/a) + \frac{P}{\Gamma}. \tag{9}$$

The amplitude C is determined by the boundary conditions, for example, $\Delta\rho = 0$ at $r = R$ for completely depolarizing walls yields $C = -P[\Gamma I_0(R/a)]^{-1}$. The characteristic length scale $a = \sqrt{D/\Gamma}$ is set by optical pumping, relaxation, and diffusion. For Cs diffusing in 10 Torr N_2 gas at 27 °C, $D = 7.61$ cm^2 s^{-1} [22]. We fit the spatial dependence of some representative populations with modified Bessel functions; the best fit curves are shown in Fig. 7, along with the fit parameters Γ.

The nuclear- and electron-spin projections produced by optical pumping are parallel for allowed-transition pumping, but opposite for forbidden-transition pumping. For the same pump intensity, allowed-transition pumping induced an order-of-magnitude-greater electron-spin polarization in the vapor, but roughly the same nuclear-spin polarization. We calculated the total spin currents to the cylindrical sidewalls of the cells (with $R = 1.1$ cm, $\ell = 5.7$ cm) to be $I_S = -6.7 \times 10^{12}\,\hbar\,\mathrm{s}^{-1}$ and $I_I = -2.5 \times 10^{12}\,\hbar\,\mathrm{s}^{-1}$ for allowed-transition pumping and $I_S = -6.8 \times 10^{11}\,\hbar\,\mathrm{s}^{-1}$ and $I_I = +1.8 \times 10^{12}\,\hbar\,\mathrm{s}^{-1}$ for forbidden-transition pumping.

E. Pump intensity dependence

We also measured the dependence of the populations in the vapor on the incident pump intensity near the symmetry axis of the vapor cell. The results of these measurements for the pumping transitions depicted in Fig. 4 are shown in Fig. 8,

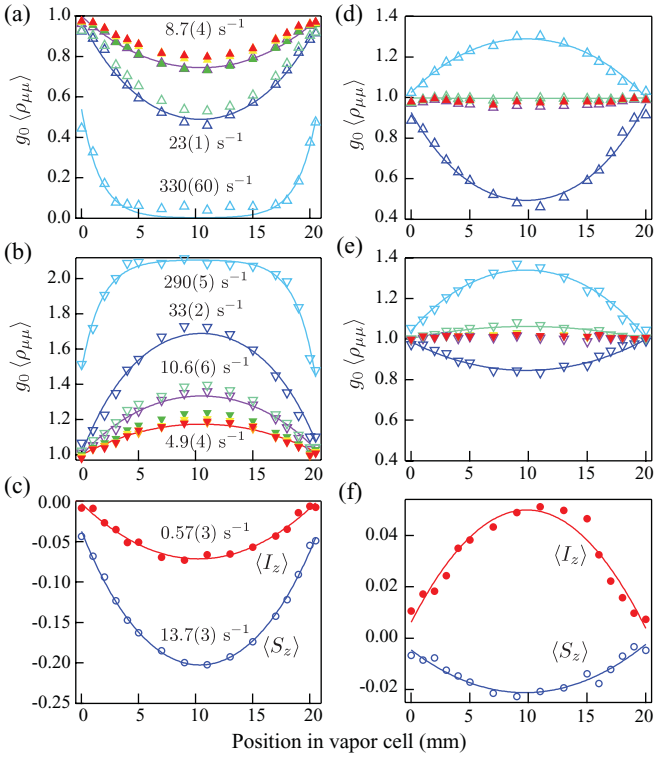

FIG. 7. (Color online) Dependence of the sublevel populations and spin projections $\langle I_z\rangle$ and $\langle S_z\rangle$ on position along a diameter of the cylindrical vapor cell (see Fig. 4 for symbol definitions). The walls of the cell are approximately at the edges of the plots, at 0 and 21 mm. The individual sublevel populations and spin projections are consistent with a simple diffusion model for an infinitely long cylinder where the vapor is completely depolarized ($g_0\langle\rho_{\mu\mu}\rangle = 1$) at the cell wall. (a) and (d) show the normalized sublevel populations with $m_S = +\frac{1}{2}$ for allowed and forbidden pumping, respectively. (b) and (e) similarly show the sublevel populations with $m_S = -\frac{1}{2}$ and (c) and (f) show the nuclear- and electron-spin projections, respectively. Fit parameters Γ are shown for some representative traces in (a)–(c).

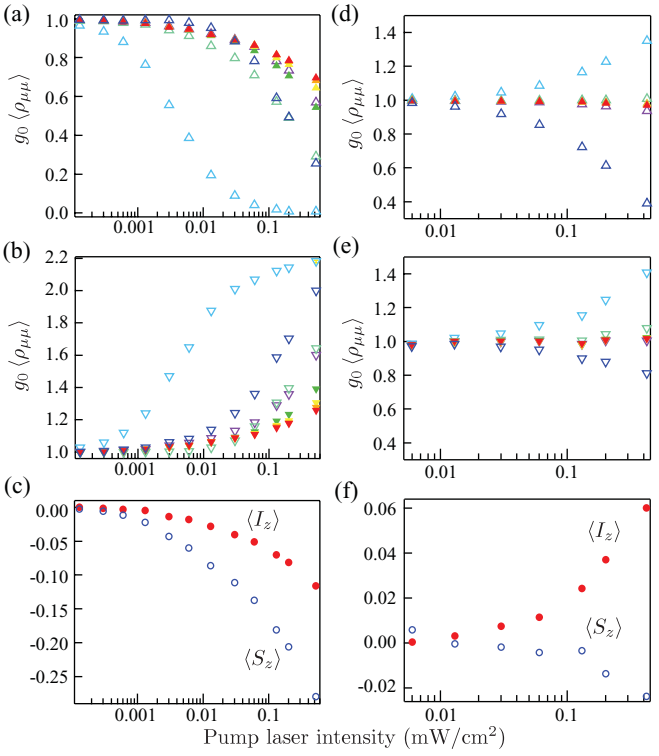

FIG. 8. (Color online) Dependence of the sublevel populations and spin projections $\langle I_z\rangle$ and $\langle S_z\rangle$ on incident pump intensity. (a) and (d) show the normalized sublevel populations with $m_S = +\frac{1}{2}$ for allowed and forbidden pumping, respectively. (b) and (e) similarly show the sublevel populations with $m_S = -\frac{1}{2}$ and (c) and (f) show the spin projections for allowed and forbidden pumping, respectively.

where the horizontal axis is the pump intensity measured by the optical power meter.

F. Pump frequency dependence

In the preceding sections we discussed the change in populations in a Cs vapor due to optical pumping at only a pair of frequencies. We also measured the change in populations in the vapor over the entire range of pump frequencies: At each pump frequency, we measured a dark and a pumped spectrum for both ground-state manifolds and extracted all 16 ground-state populations $\langle\rho_{\mu\mu}\rangle$ for a probe beam near the symmetry axis of the cell. The pump power was kept constant throughout the series of measurements by slightly adjusting the optical fiber input coupling efficiency. In Fig. 9 we compare the nuclear and electronic polarizations induced in the vapor by D_2 pumping on all transitions for vapor cells with different buffer-gas contents: 10 Torr He, 10 Torr N_2, and 40 Torr N_2. We see that the expectation of the electron-spin projection $\langle S_z\rangle$ on resonance is smallest for the cell with He buffer gas and only about 50% larger for the cell with 40 Torr N_2 buffer gas. The nuclear-spin projection $\langle I_z\rangle$, however, increases by more than an order of magnitude. The magnitude of nuclear polarization induced in the vapor is roughly proportional to the rate of hyperfine-shift damping induced by alkali-metal-atom–buffer-gas collisions based on a measured rate for Cs-N_2 [23] and a theoretical estimate for Cs-He [24].

Alkali-metal atoms are subject to two perturbations during collisions with buffer-gas particles and with other alkali-metal atoms. The first, called the spin-rotation interaction, couples the alkali-metal electron spin **S** and the alkali-metal–buffer-gas pair's orbital angular momentum **N**:

$$V_{\rm sr} = \gamma' \mathbf{N}\cdot\mathbf{S}. \tag{10}$$

The spin-rotation interaction leads to damping of the electron spin in the alkali-metal vapor, with characteristic rate $\Gamma_{\rm sr}$. The other significant interaction during collisions is the hyperfine-shift interaction, which perturbs the coupling between the alkali-metal nuclear spin **I** and electron spin **S**:

$$V_{\rm hfs} = \delta A \mathbf{I}\cdot\mathbf{S}. \tag{11}$$

The hyperfine-shift interaction has a characteristic rate $\Gamma_{\rm hfs}$, also known as the Carver rate [24,25], and, in the nearly decoupled conditions of our experiments, tends to equalize the populations of sublevels with the same total spin projection $m = m_I + m_S$. Gases with large Carver rates such as N_2

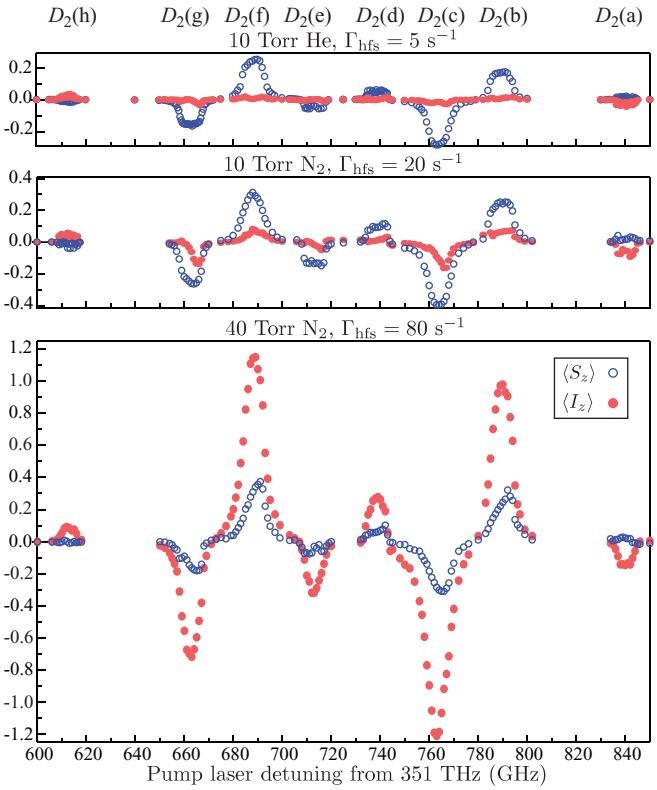

FIG. 9. (Color online) Measured pump frequency dependence of the spin projections $\langle S_z \rangle$ [open (blue) circles] and $\langle I_z \rangle$ [solid (red) circles] near the center of the cell. For the singly forbidden transitions D_2(a) and D_2(h), the nuclear and electronic polarizations had opposite sign, while for the allowed transitions, they had the same sign. As the hyperfine-shift damping rate Γ_{hfs} increased, the electron-spin projection $\langle S_z \rangle$ increased by about 50%, but the nuclear-spin projection $\langle I_z \rangle$ increased by more than an order of magnitude.

ensure better spin transfer rates than gases such as Ar with exceptionally small Carver rates.

III. THEORY

The model used to analyze our experimental results is summarized briefly in the following sections. It is based on the formalism developed in Ref. [20]; we will refer to the relevant sections of that book when the details of our model are too lengthy for inclusion in this paper.

A. Density-matrix evolution

In Liouville space, the evolution of the density matrix $|\rho)$ for an alkali-metal vapor within a buffer gas undergoing diffusive motion with coefficient D is given by

$$\frac{\partial}{\partial t}|\rho) = (D\nabla^2 - G)|\rho), \tag{12}$$

where the spin-evolution operator G has components due to the atomic Hamiltonian, collisions, and atom-light interactions:

$$G = G_H + G_c + G_{op}. \tag{13}$$

Each contribution G_x to the evolution operator can be written as a characteristic rate Γ_x multiplied by a dimensionless operator containing the details of the relaxation $G_x = \Gamma_x A_x$. We will give representative rates for the most important components for the case of Cs in 10 Torr N_2 buffer gas at 27 °C (for more detail, see Ref. [26]). The component that describes the effects of collisions is a sum of subcomponents for three relaxation mechanisms:

$$G_c = G_{sd} + G_{hfs} + G_{se}, \tag{14}$$

where G_{sd} describes S-damping relaxation, which comes mostly from the spin-rotation interaction of Eq. (10) and has a characteristic rate $\Gamma_{sd} = 5.4$ s^{-1} [27] (see Sec. 6.8.1 of Ref. [20]), and G_{hfs} describes damping due to the hyperfine-shift interaction of Eq. (11), with characteristic rate $\Gamma_{hfs} = 9.8$ s^{-1} [23] (see Sec. 10.7 of Ref. [20]). At high magnetic fields, when the Larmor period is comparable to the characteristic time for binary collisions, these rates are suppressed by about a factor of 2 [28,29].

The component G_{se}, which describes electron-electron spin-exchange between alkali-metal-atom pairs, depends on the local expectation of the electron spin $\langle \mathbf{S} \rangle$ and has a characteristic rate $\Gamma_{se} = 19$ s^{-1} [30] (see Sec. 10.12 of Ref. [20]). Other spin interactions, for example, with the nuclear spin of the buffer-gas atoms or molecules, are negligibly small.

In the $P_{1/2}$ and $P_{3/2}$ excited states, the atoms also undergo relaxation due to collisions with the buffer gas. Similar to S-damping in the ground state, excited-state atoms undergo J-damping collisions, with characteristic rates estimated to be $\Gamma_{jd1} = 7 \times 10^7$ s^{-1} and $\Gamma_{jd2} = 2 \times 10^8$ s^{-1} for $P_{1/2}$ and $P_{3/2}$ atoms, respectively (based on measurements with Rb [31]). Atoms can also be transferred between excited states in fine-structure-changing collisions, with a characteristic rate for $P_{3/2} \rightarrow P_{1/2}$ of $\Gamma_{c12} = 6.1 \times 10^7$ s^{-1} [32] (see Sec. 10.14 of Ref. [20]). Fine-structure-mixing rates are much smaller for noble gases than they are for N_2 [33].

B. Optical pumping

The evolution operator for optical pumping G_{op} is a sum of operators G_{dp} and G_{rp} due to depopulation and repopulation pumping, respectively, which both depend on the intensity of optical pumping light [34]. In our experiment light of temporal frequency ω and spatial frequency $k = \omega/c$ propagates along the z axis and can be written as a sum of negative- and positive-frequency parts:

$$\mathbf{E} = \tilde{\mathbf{E}} e^{i(kz-\omega t)} + \tilde{\mathbf{E}}^* e^{-i(kz-\omega t)}. \tag{15}$$

In what follows we will use a tilde to indicate complex amplitudes. We define the polarization unit vector of the light by

$$\mathbf{e} = \tilde{\mathbf{E}}/|\tilde{\mathbf{E}}|. \tag{16}$$

In the conditions of our experiments, stimulated emission is negligible, so we write the repopulation pumping matrix for D_2 pumping as [see Eq. (6.71) of Ref. [20]]

$$\tilde{G}_{rp} = \tilde{G}_{02}\, \tilde{G}_{22}^{-1}\, \tilde{G}_{20}. \tag{17}$$

The operator describing transfer from the ground state to the $P_{3/2}$ excited state is $\tilde{G}_{20}$ [see Eq. (6.23) of Ref. [20]]. The operator describing evolution within the excited state, $\tilde{G}_{22}$, includes contributions from the Hamiltonian in the excited

state and collisions, including fine-structure-changing collisions. The operator describing transfer from the excited state to the ground state, $\tilde{G}_{02}$, has contributions from spontaneous emission with characteristic rate $1/\tau_2 = 3.3 \times 10^7$ s^{-1} (see Sec. 5.3 of Ref. [20]) and from nonradiative quenching collisions with characteristic rate $\Gamma_q = 1.3 \times 10^8$ s^{-1} [35]. The quenching rate is negligibly small for collisions with noble gases and is only important for molecular gases such as N_2. On resonance, the characteristic rate $\Gamma_{\rm op}$ for optical pumping is $\approx$200 s^{-1} for light with an intensity of 0.2 mW/cm^2.

C. Laser beam propagation

The electric-field amplitude $\tilde{\mathbf{E}}$ changes as the light propagates through a vapor of atomic number density n according to the differential equation (Sec. 8.6 of Ref. [20])

$$\frac{\partial \tilde{\mathbf{E}}}{\partial z} = i2\pi n \frac{\omega}{c} \langle \boldsymbol{\alpha}_\perp \rangle \cdot \tilde{\mathbf{E}}, \tag{18}$$

where $\langle \boldsymbol{\alpha}_\perp \rangle$ is the transverse polarizability. The Hermitian part of the polarizability is proportional to the absorption cross section of Eq. (3). The eigenvectors of $\langle \boldsymbol{\alpha}_\perp \rangle$ in our experiment are σ_+ and σ_- polarization with corresponding eigenvalues $\langle \alpha_+ \rangle$ and $\langle \alpha_- \rangle$, so we have

$$\begin{aligned} \frac{\partial \tilde{E}_\pm}{\partial z} &= i2\pi n \frac{\omega}{c} \langle \alpha_\pm \rangle \tilde{E}_\pm, \\ \tilde{E}_\pm &= \tilde{E}_{\pm,0} \exp\left[i2\pi n \frac{\omega}{c} \int \langle \alpha_\pm \rangle dz \right], \end{aligned} \tag{19}$$

where $\tilde{E}_\pm = \tilde{E}_x \pm i\tilde{E}_y$ are the amplitudes for $\sigma_\pm$ light. By integrating the polarizability, we find the spatial dependence of the pump light intensity and then we calculate the optical pumping operators following the procedure summarized in Sec. III B.

D. Numerical simulation

Due to the inhomogeneity of optical pumping and spin exchange, we simulated the evolution of the density matrix at a set of discrete spatial positions. We took advantage of the cylindrical symmetry of our system and defined a two-dimensional grid of density matrices $|\rho_{i,j})$, where i and j indicate the spatial positions of a cylindrical coordinate system,

$$\begin{aligned} [r_i, z_j] &= \left[R\frac{i-1}{n_r - 1}, \ell \frac{j-1}{n_z - 1} \right] \\ \text{for} \quad i &= 1,2,\ldots,n_r, \quad j = 1,2,\ldots,n_z. \end{aligned} \tag{20}$$

We assumed no dependence on the azimuthal angle θ. We numerically integrated the diffusion equation [Eq. (12)] by explicitly solving the spatial dependence of the populations at each time step using finite-difference formulas for the spatial derivatives (see Sec. 3.1.8 of Ref. [26]). For example, we computed the axial second derivative with the algorithm

$$\frac{\partial^2 |\rho_{i,j})}{\partial z^2} = \frac{|\rho_{i,j+1}) + |\rho_{i,j-1}) - 2|\rho_{i,j})}{2\Delta\ell^2}, \tag{21}$$

where $\Delta\ell = \ell/(n_z - 1)$. We enforced the boundary condition

$$\rho_{\mu\mu} = g_0^{-1} = [(2S+1)(2I+1)]^{-1} = \tfrac{1}{16} \tag{22}$$

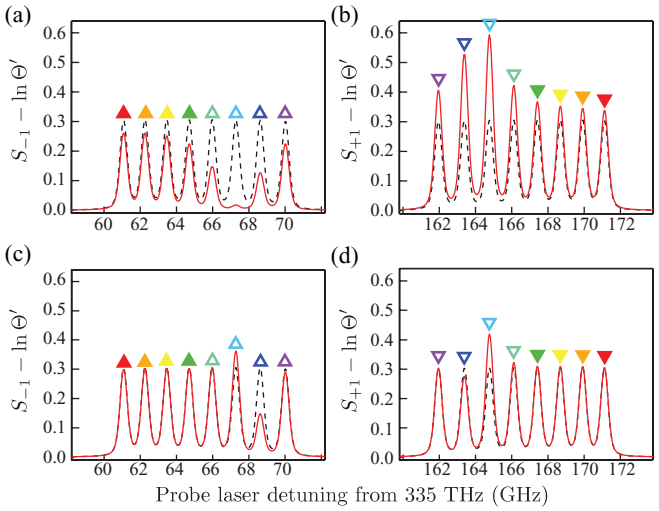

FIG. 10. (Color online) Simulated absorption spectra of Cs vapor in 10 Torr N_2 buffer gas at 27 °C (compare to experimental data in Fig. 6). The probe beam passed through the center of a cylindrical cell with $R = 1.1$ cm and $\ell = 5.7$ cm. (a) and (b) show absorption of σ_- and σ_+ probe light, respectively, for pumping on the allowed transition D_2(g) depicted in Fig. 4; (c) and (d) show absorption of σ_- and σ_+ probe light, respectively, for pumping on the forbidden transition D_2(h). The dashed (black) traces show absorption with the pump light off and the solid (red) traces show absorption with the pump light on. See Fig. 4 for symbol definitions.

at the cell walls and $\partial\rho_{\mu\mu}/\partial r = 0$ along the symmetry axis. Comparing the simulated absorption spectra for steady-state solutions in Fig. 10 to the measured absorption spectra of Fig. 6, we see very good agreement for both the unpolarized and optically pumped vapors.

Our observations agree with other experiments at high magnetic field [19], but our interpretation of the results is different from theirs. In that work, Luo *et al.* used a simple coupled-rate model for the sublevel populations in an optically pumped Cs vapor at 1.516 T. They introduced a relatively large nuclear spin-flip transition rate induced by wall relaxation to account for observational data at certain pump laser frequencies. There is no obvious physical interaction, analogous to the spin-rotation interaction [Eq. (10)] or the hyperfine shift interaction [Eq. (11)], that would lead to nuclear spin-flip transitions at the cell walls. When an optically pumped atom striking the wall is replaced by a newly evaporated atom with neither electron- nor nuclear-spin polarization, both spins are completely depolarized. Forbidden transitions with $\Delta m_I \neq 0$ at 1.516 T would have been even more prominent than in our experiments, but Luo *et al.* do not mention forbidden transitions. We suggest that unrecognized pumping of forbidden transitions may have produced the phenomena they modeled with a nuclear spin-flip transition rate.

E. Spatial dependence

We simulated the spatial dependence of the sublevel populations $\langle \rho_{\mu\mu} \rangle$ and the spin projections $\langle S_z \rangle$ and $\langle I_z \rangle$, which are shown in Fig. 11. Comparing these simulated results to the experimental data in Fig. 7, we see very good agreement. Our simulations agree well with the observed data, with maximum

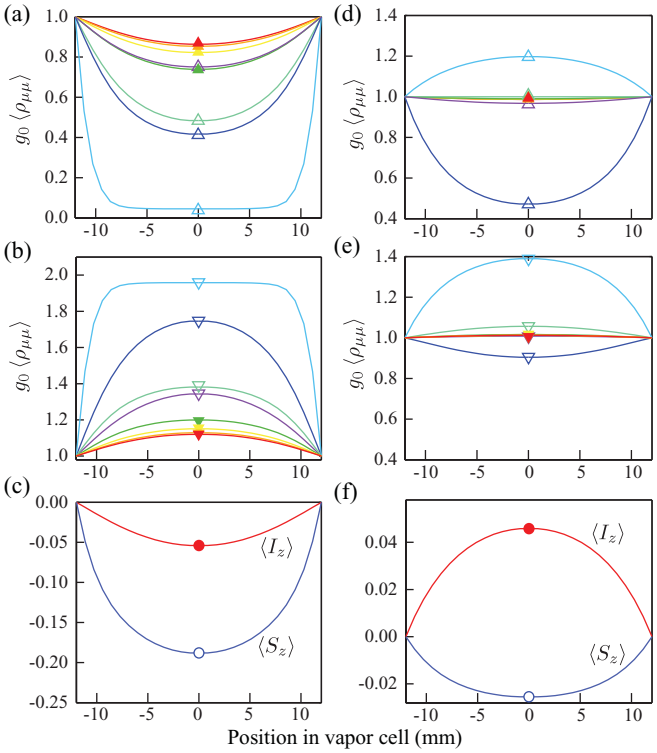

FIG. 11. (Color online) Simulated dependence of the sublevel populations $\langle\rho_{\mu\mu}\rangle$ and spin projections $\langle I_z\rangle$ and $\langle S_z\rangle$ along a diameter of the cylindrical vapor cell (compare to experimental data in Fig. 7). The walls of the cell are at the edges of the plots. (a) and (d) show the normalized sublevel populations with $m_S = +\frac{1}{2}$ for allowed and forbidden pumping, respectively. (b) and (e) similarly show the sublevel populations with $m_S = -\frac{1}{2}$ and (c) and (f) show the spin projections for allowed and forbidden pumping, respectively.

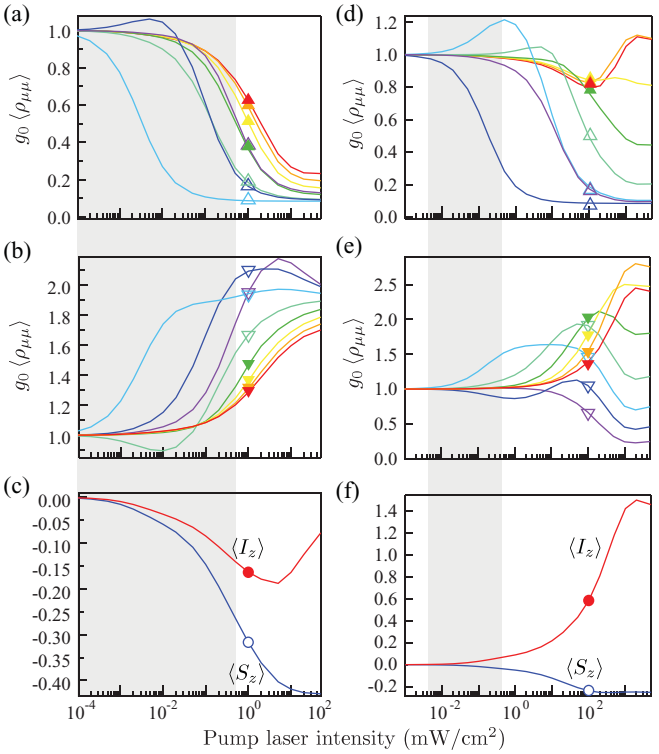

FIG. 12. (Color online) Simulated dependence of the sublevel populations $\langle\rho_{\mu\mu}\rangle$ and spin projections $\langle I_z\rangle$ and $\langle S_z\rangle$ on incident pump intensity (compare the gray regions to experimental data in Fig. 8). (a) and (d) show the normalized sublevel populations with $m_S = +\frac{1}{2}$ for allowed and forbidden pumping, respectively. (b) and (e) similarly show the sublevel populations with $m_S = -\frac{1}{2}$ and (c) and (f) show the spin projections for allowed and forbidden pumping, respectively.

deviations of about 10%. These deviations could be explained by a buffer-gas density about 5% higher than that expected from the measured filling pressure of 10 Torr.

F. Pump intensity dependence

We also simulated the dependence of the populations in the optically pumped vapor on the pump laser intensity for the two representative pumping transitions D_2(g) and D_2(h) shown in Fig. 4. The plots in Fig. 12 show the ground-state populations $\langle\rho_{\mu\mu}\rangle$ and the spin projections $\langle S_z\rangle$ and $\langle I_z\rangle$ averaged along the symmetry axis of a cell with 10 Torr N_2 buffer gas. We see that the simulated populations agree well with those we observed, except for the populations of two sublevels. Our simulations predict that $|\frac{1}{2}, -\frac{5}{2}\rangle$ [upward (dark blue) triangle] will switch from being overpopulated ($g_0\langle\rho_{\mu\mu}\rangle > 1$) at low pump intensities to being underpopulated ($g_0\langle\rho_{\mu\mu}\rangle < 1$) for pump intensities greater than 10^{-2} mW/cm^2 [see Fig. 12(a)]. Similarly, we predict that $|-\frac{1}{2}, -\frac{1}{2}\rangle$ [downward (light green) triangle] will switch from being underpopulated at low pump intensities to being overpopulated [see Fig. 12(b)]. In our experiment, summarized in Fig. 8, these two states' populations were the only two that crossed over their neighbors', though they never switched from overpopulation to underpopulation or vice versa. This discrepancy remains an open question and does not seem to have much effect on the resulting spin projections, which show good agreement between simulation and experiment.

One interesting prediction of our simulations is that the nuclear-spin projection, and hence the nuclear-spin current to the walls, reaches its maximum amplitude for a pump intensity near 5 mW/cm^2 for allowed-transition pumping [Fig. 12(c)] and 5 W/cm^2 for forbidden-transition pumping [Fig. 12(f)]. At higher intensities, the allowed-transition pump beam depopulates all of the sublevels in the $m_S = +\frac{1}{2}$ manifold nearly equally, resulting in less nuclear-spin polarization. Since the pump intensities in the SEOP experiments performed with CsH were on the order of 100 mW/cm^2 [14], they may have induced smaller-than-optimal nuclear-spin currents to the wall. However, at such high pump intensities, our assumption of negligible stimulated emission begins to break down.

G. Pump frequency dependence

In Fig. 13 we show simulations of the nuclear- and electronic-spin projections $\langle I_z\rangle$ and $\langle S_z\rangle$ as functions of pump laser frequency. For all of the transitions except D_2(d) and D_2(e), the simulated spin projections in Fig. 13 agree very well with observed spin projections of Fig. 9. For the two singly forbidden transitions D_2(d) and D_2(e), however, our simulations are qualitatively different from

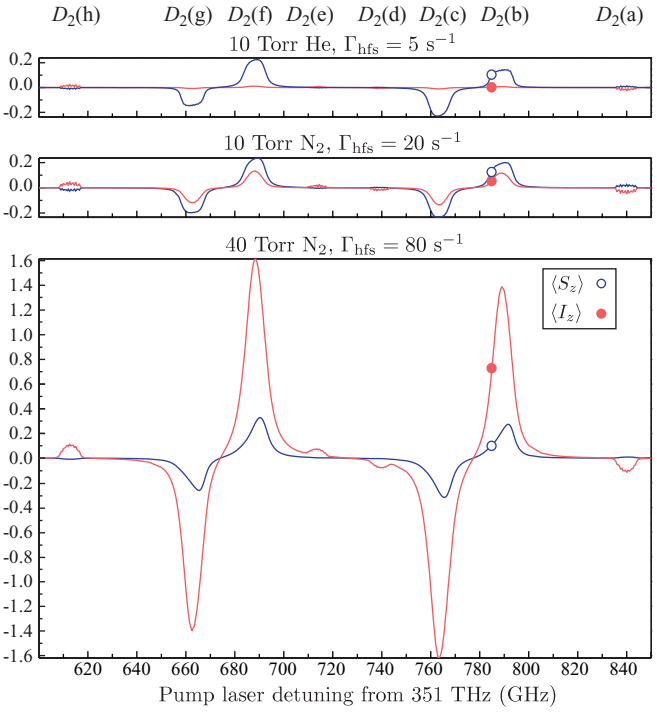

FIG. 13. (Color online) Simulated dependence of the spin projections $\langle S_z \rangle$ and $\langle I_z \rangle$ on the frequency of the pump laser (compare to experimental data in Fig. 9). For the singly forbidden transitions D_2(a) and D_2(h), the nuclear (light red) and electronic (dark blue) polarizations had opposite sign, while for the allowed transitions, they had the same sign. As the hyperfine-shift damping rate $\Gamma_{\rm hfs}$ increased, the electron-spin projection $\langle S_z \rangle$ increased by about 50%, but the nuclear-spin projection $\langle I_z \rangle$ increased by more than an order of magnitude.

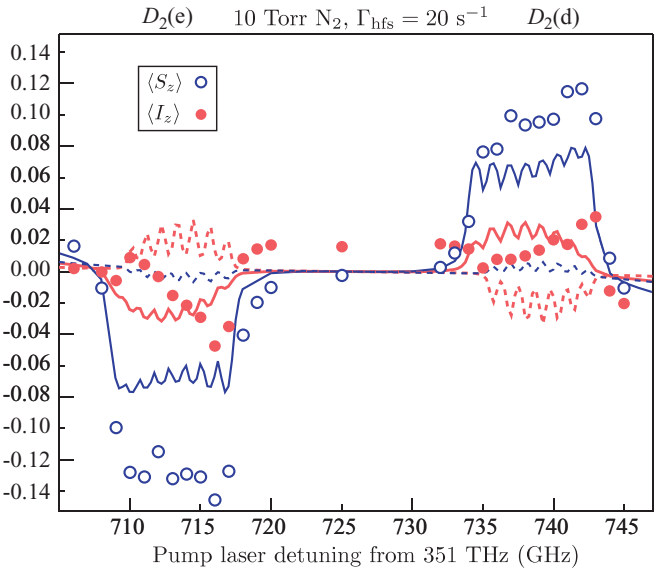

FIG. 14. (Color online) Experimentally observed and simulated pump frequency dependence of the spin projections $\langle S_z \rangle$ (dark blue) and $\langle I_z \rangle$ (light red) for a cell with 10 Torr N_2 buffer gas. The dashed curves are results from the simulation neglecting fluorescence and the solid curves are simulations with an artificial component of π-polarized light introduced. The simulation with this simple treatment of fluorescence agrees qualitatively with the experimental data, while the simulation without fluorescence predicts the wrong sign for $\langle I_z \rangle$.

the spin projections we observed. In all three cases, we observed $\langle S_z \rangle \approx \pm 0.1$ for these two transitions, while our simulations predict $\langle S_z \rangle = 0$. We also see that the sign of $\langle I_z \rangle$ predicted by our simulations is opposite the observed sign. This discrepancy is likely due to an effect not included in our simulations: optical pumping by fluorescent photons that are recaptured by the vapor, also known as radiation trapping [36,37].

Consider optical pumping on the singly forbidden transition D_2(d). The incoming light is linearly polarized perpendicular to the magnetic field, with nearly equal components of σ_+ and σ_- light (see Fig. 2); only the σ_- light is absorbed by the vapor, so the σ_+ light passes through the cell. The atoms excited by the pump light into the $P_{3/2}$ level will decay via spontaneous emission to the ground state with rate $1/\tau_2$, via level-changing collisions to the $P_{1/2}$ level with rate Γ_{c12} and via quenching collisions with the buffer gas with rate Γ_q, as discussed in Sec. III A. In the case of a cell with 10 Torr N_2, spontaneous emission accounts for

$$\frac{1/\tau_2}{1/\tau_2 + \Gamma_{c12} + \Gamma_q} = 15\% \tag{23}$$

of the deexcitation of excited atoms from the $P_{3/2}$ level. This will lead to a significant amount of fluorescent light in the cell. The rate of emission of fluorescent photons is proportional to $|\mathbf{D} \cdot \mathbf{e}_\lambda|^2$, so the majority of fluorescent photons will have polarization index λ corresponding to the polarization with greatest absorption cross section σ_λ (see Fig. 5).

For optical pumping on allowed transitions, the fluorescent light will be mostly polarized the same as the incident light, but for pumping on a singly forbidden transition, the fluorescent light will mostly be polarized according to the allowed transition at that frequency [π in the case of D_2(d)]. We suspect the resulting polarization mixing will be strongest near the cell walls, where the incident pump light will be most strongly attenuated due to absorption by the nearly unpolarized vapor. The recapture of fluorescent photons should then have a large effect on the nuclear-spin current to the cell walls for the transitions D_2(d) and D_2(e), which would strongly influence the NMR enhancement of Cs salts [15].

As a simplistic model for fluorescent light, we simulated a pump beam with an artificial component of π-polarized light added. We changed the simulated axis of the beam to allow the π-polarized light to propagate according to Eq. (18). In Fig. 14, we compare the results of the simulations with and without π-polarized light to experimental data. The electron- and nuclear-spin projections we observed match the simulations involving uniform illumination with fluorescent light fairly well; we expect a more sophisticated simulation of fluorescence will improve this agreement.

IV. CONCLUSION

We have developed an experimental apparatus to perform absorption spectroscopy measurements on a Cs vapor at high magnetic field to measure all 16 ground-state sublevel

populations while selectively depopulating a single sublevel. We found that the populations exhibit simple spatial diffusion shapes, leading to nuclear- and electronic-spin currents to the cell walls. We developed a numerical simulation of this system and found that the observed populations in the vapor were consistent with known relaxation mechanisms. Except for forbidden transitions where the dominant fluorescence polarization differs from the pump polarization, our models closely reproduce the observed behavior in the vapor. Using cells filled with different noble gases in our apparatus, we should be able to measure the hyperfine-shift damping rates Γ_{hfs} for Cs–noble-gas collisions, which have not yet been measured.

ACKNOWLEDGMENTS

The authors would like to thank M. Souza for assistance with glass cell construction and Dr. K. Ishikawa for numerous illuminating discussions. This work was supported by the US Air Force Office of Scientific Research.

[1] J. A. Crosse and S. Scheel, Phys. Rev. A **79**, 062902 (2009).
[2] H. de Freitas, M. Oria, and M. Chevrollier, Appl. Phys. B **75**, 703 (2002).
[3] K. Zhao and Z. Wu, Phys. Rev. A **71**, 012902 (2005).
[4] J. Kitching, S. Knappe, L. Liew, J. Moreland, P. D. D. Schwindt, V. Shah, V. Gerginov, and L. Hollberg, Metrologia **42**, S100 (2005).
[5] F. Gong, Y.-Y. Jau, K. Jensen, and W. Happer, Rev. Sci. Instrum. **77**, 076101 (2006).
[6] A. Post, Ph.D. thesis, Princeton University, 2006.
[7] P. D. D. Schwindt, B. Lindseth, S. Knappe, V. Shah, J. Kitching, and L.-A. Liew, Appl. Phys. Lett. **90**, 081102 (2007).
[8] E. J. Eklund, A. M. Shkel, S. Knappe, E. Donley, and J. Kitching, Sensors Actuators A **143**, 175 (2008).
[9] F. Franz, T. Marshall, and J. Munarin, Phys. Lett. **36A**, 31 (1971).
[10] T. R. Marshall, R. Boggy, and F. A. Franz, Phys. Rev. A **16**, 618 (1977).
[11] J. Guiry and L. Krause, Phys. Rev. A **12**, 2407 (1975).
[12] M. Augustine and K. Zilm, J. Chem. Phys. **105**, 2998 (1996).
[13] M. P. Augustine and K. W. Zilm, Chem. Phys. Lett. **280**, 24 (1997).
[14] K. Ishikawa, B. Patton, Y.-Y. Jau, and W. Happer, Phys. Rev. Lett. **98**, 183004 (2007).
[15] K. Ishikawa, B. Patton, B. A. Olsen, Y.-Y. Jau, and W. Happer, Phys. Rev. A **83**, 063410 (2011).
[16] B. Patton, Ph.D. thesis, Princeton University, 2007 [http://www.princeton.edu/physics/academics/graduate-program/theses/theses-from-2007/].
[17] K. Ishikawa, Phys. Rev. A **84**, 033404 (2011).
[18] A. W. Overhauser, Phys. Rev. **92**, 411 (1953).
[19] J. Luo, X.-P. Sun, X.-Z. Zeng, and M.-S. Zhan, Chin. Phys. **16**, 998 (2007).
[20] W. Happer, Y.-Y. Jau, and T. Walker, *Optically Pumped Atoms* (Wiley-VCH, Weinheim, 2010).
[21] G. B. Arfken and H. J. Weber, *Mathematical Methods for Physicists*, 5th ed. (Harcourt Academic, San Diego, 2001).
[22] N. Beverini, P. Minguzzi, and F. Strumia, Phys. Rev. A **4**, 550 (1971).
[23] Y.-Y. Jau, Ph.D. thesis, Princeton University, 2004 [http://www.princeton.edu/physics/academics/graduate-program/theses/theses-from-2004/].
[24] J. C. Camparo, J. Chem. Phys. **126**, 244310 (2007).
[25] D. K. Walter, W. M. Griffith, and W. Happer, Phys. Rev. Lett. **88**, 093004 (2002).
[26] B. A. Olsen, Ph.D. thesis, Princeton University, 2011 [http://www.princeton.edu/physics/graduate-program/theses/theses-from-2011-1/].
[27] F. A. Franz and C. E. Sooriamoorthi, Phys. Rev. A **10**, 126 (1974).
[28] S. Kadlecek, T. Walker, D. K. Walter, C. Erickson, and W. Happer, Phys. Rev. A **63**, 052717 (2001).
[29] Y.-Y. Jau, N. N. Kuzma, and W. Happer, Phys. Rev. A **67**, 022720 (2003).
[30] N. W. Ressler, R. H. Sands, and T. E. Stark, Phys. Rev. **184**, 102 (1969).
[31] M. D. Rotondaro and G. P. Perram, Phys. Rev. A **58**, 2023 (1998).
[32] G. A. Pitz, C. D. Fox, and G. P. Perram, Phys. Rev. A **84**, 032708 (2011).
[33] M. Czajkowski, D. A. McGillis, and L. Krause, Can. J. Phys. **44**, 91 (1966).
[34] W. Happer, Rev. Mod. Phys. **44**, 169 (1972).
[35] D. A. McGillis and L. Krause, Can. J. Phys. **46**, 1051 (1968).
[36] D. Tupa, L. W. Anderson, D. L. Huber, and J. E. Lawler, Phys. Rev. A **33**, 1045 (1986).
[37] L. Anderson and T. Walker, Nucl. Instrum. Methods Phys. Res. Sect. A **316**, 123 (1992).